https://doi.org/10.5194/egusphere-2024-472
Preprint. Discussion started: 27 February 2024

A nonhydrostatic formulation for MPAS-Ocean

Sara Calandrini[1], Darren Engwirda[1], and Luke Van Roekel[1]
[1]Theoretical Division, Los Alamos National Laboratory, Los Alamos, NM, U.S.A.
Correspondence: Sara Calandrini (scalandrini@lanl.gov)

Abstract. The Model for Prediction Across Scales-Ocean (MPAS-Ocean) is an open-source, global ocean model and is one component of a family of climate models within the MPAS framework, including atmosphere, sea-ice, and land-ice models. In this work, a new formulation for the ocean model is presented that solves the nonhydrostatic, incompressible Boussinesq equations on an unstructured, staggered, z-level grid. The introduction of this nonhydrostatic capability is necessary for the resolution of internal wave dynamics and large eddy simulations. Compared to the standard, hydrostatic formulation, a nonhydrostatic pressure solver and a vertical momentum equation are added, where the PETSc (Portable Extensible Toolkit for Scientific Computation) library is used for the inversion of a large sparse system for the nonhydrostatic pressure. Numerical results on a stratified seiche, internal solitary wave, overflow and lock-exchange test cases are presented, and the parallel efficiency of the code is evaluated using up to 128 processors.

1 Introduction

Most modern ocean circulation models adopt the hydrostatic pressure assumption, i.e. they assume that the pressure at any point in the ocean is due to the weight of the water above it. For global ocean simulations, where the horizontal scale is considerably larger than the vertical, such an assumption is legitimate since the variability in pressure is due primarily to the hydrostatic pressure arising from the weight of the fluid above a point beneath the water surface. Mathematically, the hydrostatic approximation consists in (i) a simplification of the equation governing the vertical component of velocity, by neglecting terms associated with large and fast vertical motion, and (ii) the elimination of the nonhydrostatic pressure contribution from the pressure term. When moving from global ocean simulations to smaller scaled oceanic phenomena, such as the breaking of internal waves, convection, and shear-induced overturning, the missing piece of physics comes into account, as hydrostatic models don't do a good job in simulating processes over shorter horizontal scales relative to the depth. For such regional, smaller scaled processes nonhydrostatic effects become important, creating the need to include the nonhydrostatic pressure.

Nowadays, nonhydrostatic models have been developed for both structured grid, as MITgcm [Marshall et al. (1997)], CROCO [Auclair et al. (2018)], GETM [Klingbeil and Burchard (2013)], and unstructured grid, like UnTRIM [Casulli (1999)], and SUNTANS [Fringer et al. (2006); Vitousek and Fringer (2014)]. SUNTANS and MITgcm use a pressure-correcting projection method to extend their hydrostatic model to a nonhydrostatic one, splitting the pressure into its hydrostatic and nonhydrostatic components. The hydrostatic velocity field that satisfies the depth-averaged continuity equation is computed first, and then it is corrected with the nonhydrostatic pressure field. This approach requires the solution of a 3D Poisson equation

https://doi.org/10.5194/egusphere-2024-472
Preprint. Discussion started: 27 February 2024

for the nonhydrostatic pressure, which accounts for a bulk of the workload for nonhydrostatic codes using pressure-correcting projection methods. In MITgcm, a quasi-hydrostatic option is also present where cosine-of-latitude Coriolis terms neglected in hydrostatic primitive equation models are included. The GETM model adopts a straight-forward inclusion of the missing non-
30 hydrostatic pressure contribution, that is it performs an explicit vertical integration of the additional nonhydrostatic terms within the balance of vertical momentum to then include them in the horizontal pressure gradient. The advantage of this approach is that it does not require the inversion of a Poisson equation. The CROCO model presents a three-mode time-split algorithm to simulate nonhydrostatic ocean processes, including compressible, acoustic effects. Most ocean models use a barotropic / baroclinic time-splitting [Higdon (2005)], where the 2D fast, barotropic mode is embedded in the slow, baroclinic mode. In the
35 three-mode time-split algorithm one further, compressible (non-Boussinesq) mode is implemented within the barotropic mode. Hence, together with the barotropic and baroclinic time-steps, a third splitting is employed, and is dedicated to the "very fast" time scales associated to compressible nonhydrostatic effects.

In this work, we present a new formulation for MPAS-Ocean [Ringler et al. (2013); Petersen et al. (2015); Calandrini et al. (2021)] that solves the nonhydrostatic, incompressible Boussinesq equations on an unstructured, staggered, z-level grid.
40 MPAS-Ocean is the ocean component of the U.S. Department of Energy Exascale Earth System Model (E3SM) [Petersen et al. (2019); Golaz et al. (2019)]. The introduction of this nonhydrostatic capability is necessary for the resolution of internal wave dynamics, as well as high-resolution submesoscale eddy processes important for coastal modelling applications. The nonhydrostatic version of MPAS-Ocean (MPAS-Ocean NH) is the first global nonhydrostatic model at variable resolution, (other codes are either regional nonhydrostatic models, as CROCO and SUNTANS, or global models at fixed resolution, as
45 MITgcm) and is the first nonhydrostatic ocean model to be fully coupled in a climate model. The variable resolution mesh allows us to have appropriate high resolution in defined regions and much coarser regions elsewhere, so that MPAS-Ocean NH can be used only where we expect strong vertical motions, and the hydrostatic model would be use in the majority of the domain. This makes global ocean runs with the nonhydrostatic model possible, since the more expensive nonhydrostatic solution would be computed only where needed, without dragging down the total computational time. In this paper, we present
50 the nonhydrostatic formulation for MPAS-Ocean and show its correctness on idealized benchmark test cases. As SUNTANS and MITgcm, we use a pressure-correcting projection method to extend the MPAS-Ocean hydrostatic model to a nonhydrostatic one. A vertical momentum equation is added to the classical primitive equations (3D Boussinesq equations in hydrostatic balance), together with a nonhydrostatic pressure term in the horizontal momentum equation. The 3D Poisson equation for the nonhydrostatic pressure is solved with a preconditioned conjugate gradient algorithm using the external PETSc (Portable
55 Extensible Toolkit for Scientific Computation) library [Balay et al. (2021a)], which provides data structures and routines for the parallel solution of many scientific applications modeled by partial differential equations. All MPAS-Ocean time-stepping schemes (RK4, split-explicit [Ringler et al. (2013)] and semi-implicit [Kang et al. (2021)]) have been adapted for solving the new nonhydrostatic model. In all three schemes, an implicit Euler step is performed for the treatment of the vertical diffusion present in the horizontal and vertical momentum and in the tracer equations. For all the results reported in this paper the RK4
60 time-stepping scheme has been used. We will show numerically that the presented nonhydrostatic formulation is second-order accurate in time, because the update of the nonhydrostatic pressure is second-order accurate. Similar to Fringer et al. (2006),

https://doi.org/10.5194/egusphere-2024-472
Preprint. Discussion started: 27 February 2024

an extrapolation technique is used for the nonhydrostatic pressure since it is staggered in time with respect to the velocity. The new nonhydrostatic capability of MPAS-Ocean is assessed by different benchmark test cases consisting in: (1) a continuously stratified seiche in an enclosed domain, (2) the formation of internal solitary waves, (3) the generation of a plume in an overflow scenario and (4) the formation of Kelvin–Helmholtz billows at the shear interface between two fluids of different densities. All four tests show that MPAS-Ocean NH correctly describes the behavior of highly convective flows.

This paper is organized as follows. Section 2 describes the 3D Boussinesq nonhydrostatic equations highlighting the differences with their hydrostatic counterpart. Section 3 describes the computational grid used by MPAS-Ocean, and section 4 illustrated the spatial discretization on such a grid. In section 5 the new nonhydrostatic capability is tested on four benchmark test cases, and details about the code performance are given in section 6. Finally, conclusions are drawn in section 7.

2 Formulation

The dynamics of a Boussinesq, three-dimensional, nonhydrostatic fluid in a rotating frame can be expressed in terms of the following augmented primitive equation set, in which $\pi = \pi(\mathbf{x}, t)$ denotes a general space- and time-dependent nonhydrostatic contribution to the total fluid pressure

$$\partial_t \mathbf{u}_h + (\mathbf{u}\cdot\nabla)\mathbf{u}_h + f\mathbf{u}_h^{\perp} = -\frac{1}{\rho_0}\nabla_h\,(p_h + \pi) + S_u\,, \tag{1}$$

$$\partial_t w + (\mathbf{u}\cdot\nabla)w = -\frac{1}{\rho_0}\partial_z\,\pi + S_w\,, \tag{2}$$

$$\nabla\cdot\mathbf{u} = 0\,, \quad p_h = \rho_0 g(\eta - z) + g\int_z^{\eta} \rho(T,S,p_h) - \rho_0\,\mathrm{d}z'\,, \tag{3}$$

$$\partial_t \psi + \nabla\cdot(\mathbf{u}\psi) = S_\psi\,. \tag{4}$$

Here, $\mathbf{u}_h$ and w denote the horizontal and vertical components of the fluid velocity, $\mathbf{u} = (\mathbf{u}_h, w)$ is the full three-dimensional velocity field, and ∇_h, ∂_z are horizontal and vertical gradient operators, such that $\nabla = (\nabla_h, \partial_z)$. The density of the fluid is characterised by a general temperature- and salinity-dependent equation of state $\rho(T,S,p_h)$, with ρ_0 a constant reference value associated with the Boussinesq approximation. The full fluid pressure $p = p_h + \pi$ is composed as the sum of the resulting hydrostatic pressure p_h and the nonhydrostatic component π. The system is closed noting that g is the gravitational acceleration, f is the Coriolis parameter acting on the tangential velocity field $\mathbf{u}_h^{\perp} = (v, u)$, and the tendencies S_u, S_w, S_ψ represent all remaining source, forcing, mixing and dissipative terms associated with the fluid momentum and conservative tracer variables. Such terms do not feature directly within the nonhydrostatic formulation presented here, and the reader is referred to, e.g. Ringler et al. (2013) for additional details regarding the specific implementation of these tendencies that is employed in MPAS-Ocean.

Anticipating an extension to general unstructured meshes on the sphere, we recast the horizontal momentum equation into a flexible, vector-invariant form; exploiting the identity $(\mathbf{u}_h\cdot\nabla_h)\mathbf{u}_h = (\nabla\times\mathbf{u}_h)\times\mathbf{u}_h + \nabla_h\,\frac{1}{2}\|\mathbf{u}_h\|^2$ to express the horizontal

https://doi.org/10.5194/egusphere-2024-472
Preprint. Discussion started: 27 February 2024

components of nonlinear momentum advection in terms of the equivalent kinetic-energy $K_h = \frac{1}{2}\|\mathbf{u}_h\|^2$ and relative-vorticity $\xi_h = \nabla_h \times \mathbf{u}_h$ tendencies. To further aid exposition on unstructured meshes, the advective tendencies in the vertical momentum and tracer transport equations are also decomposed into horizontal and vertical components, leading to

$$\partial_t \mathbf{u}_h + (\xi_h + f)\mathbf{u}_h^{\perp} + w\partial_z \mathbf{u}_h = -\frac{1}{\rho_0}\nabla_h (p_h + \pi) - \nabla_h K_h + S_u \,, \tag{5}$$

$$\partial_t w + (\mathbf{u}_h \cdot \nabla_h) w + w\partial_z w = -\frac{1}{\rho_0}\partial_z \pi + S_w \,, \tag{6}$$

$$\nabla \cdot \mathbf{u} = 0 \,, \quad p_h = \rho_0 g(\eta - z) + g\int_z^{\eta} \rho(T, S, p_h) - \rho_0 \,\mathrm{d}z' \,, \tag{7}$$

$$\partial_t \psi + \nabla_h \cdot (\mathbf{u}_h \psi) + \partial_z (w\psi) = S_\psi \,. \tag{8}$$

Compared to the Boussinesq hydrostatic system conventionally solved in MPAS-Ocean (see e.g. Ringler et al. (2013)), equations (5–8) contain a number of important differences, namely: (i) an explicit expression of vertical momentum balance, and (ii) additional acceleration tendencies, via the nonhydrostatic contributions to the horizontal and vertical pressure gradients in $\nabla_h \pi$ and $\partial_z \pi$. As will be explored in subsequent sections, the presence of these additional nonhydrostatic contributions have important consequences both for the dynamics resolved by the model, as well as the numerical methods required to integrate the model forward in time.

3 Computational grid

MPAS-Ocean is based on an unstructured C-grid finite-volume/difference discretization, in which the horizontal domain is subdivided into a complex of polygonal control-volumes, with the vertical domain consisting of quasi-structured vertical layers. Consistent with structured-grid models, numerical degrees-of-freedom are distributed at staggered locations throughout the mesh, with fluid height and conserved tracer variables positioned at the centres of polygonal control-volumes/fluid layers, and normally-oriented velocity components placed at horizontal cell edges and vertical layer interfaces. See Figure 1 for additional detail.

The unstructured meshes used in MPAS-Ocean are a class of orthogonal grids known as Centroidal Voronoi Tessellations (CVTs). The mathematical properties of CVTs are well known (see e.g. Du et al. (1999)), so our purpose here is only to review their salient aspects and to describe our C-grid staggering procedure. The reader is referred to, e.g. Ringler et al. (2008); Hoch et al. (2020) for additional details regarding the use of CVTs in ocean modelling. A Voronoi tessellation on a generic surface S, can be created by picking $\{x_i\}_{i=1}^n$ distinct grid points and then assigning every point on S to whichever x_i it is closest to. This results in a set of Voronoi regions, $\{V_i\}_{i=1}^n$, that can be expressed as

$$V_i = \{y \in S \text{ s.t. } ||x_i - y|| < ||x_j - y|| \text{ for } j = 1, \ldots, n \text{ and } j \neq i\} \,, \tag{9}$$

https://doi.org/10.5194/egusphere-2024-472
Preprint. Discussion started: 27 February 2024

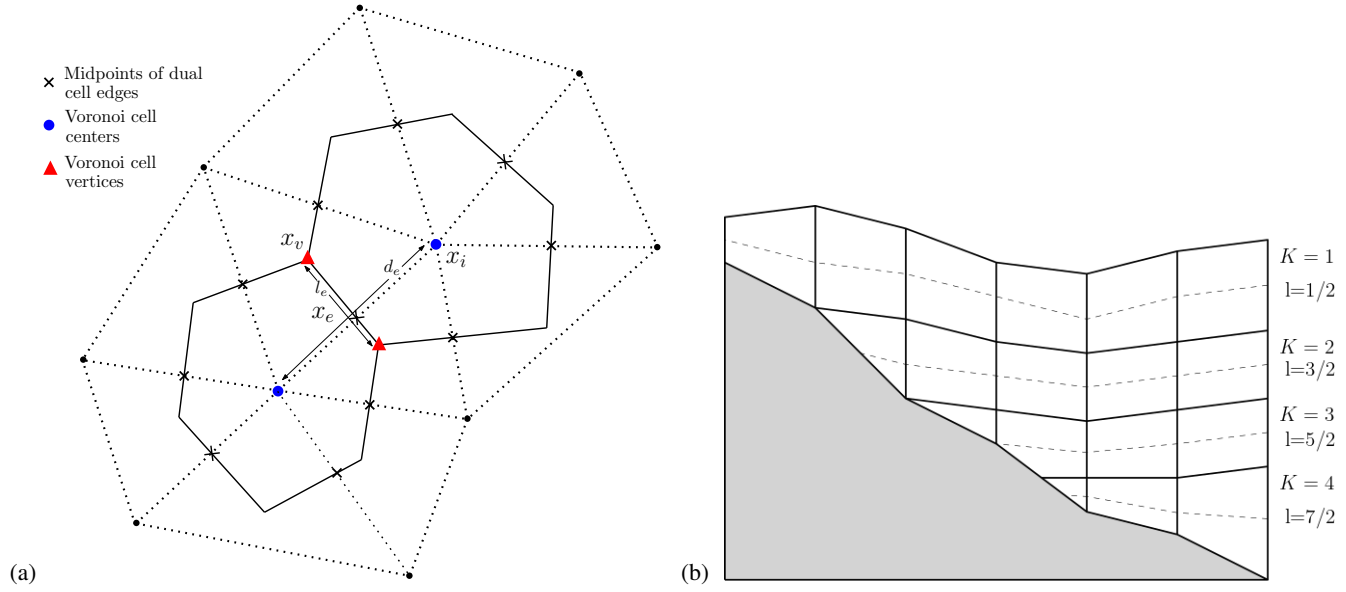

Figure 1. Collocation points for the unstructured C-grid scheme on (a) CVT meshes and (b) z^*-type vertical layering.

such that each V_i is uniquely associated with a single grid point x_i. In a CVT, the points $\{x_i\}_{i=1}^n$ are also approximations of the centroids (mass centers) of the Voronoi cells. A Voronoi tessellation is the dual-mesh of a Delaunay triangulation; specifying either uniquely determines the other. The meshes are dual in the sense that the vertices of one mesh are the centers of the other mesh, as per Fig. 1. Another important feature of these grids is orthogonality, i.e. the edges of the primal (Voronoi) mesh cells are exactly orthogonal to the dual (Delaunay) triangle edges. The JIGSAW library [Engwirda (2017)] was used to generate the various CVT meshes used throughout this study. Each Voronoi cell V_i in the horizontal mesh is associated with a vertical column of fluid layers that discretize the vertical domain from sea-surface height $\eta(\mathbf{x}, t)$ to the bottom bathymetry $b(\mathbf{x})$.

MPAS-Ocean's unstructured C-grid discretization associates fluid height, temperature, salinity and any other conserved tracers with the prismatic polygonal volumes formed by extruding the Voronoi cells in the horizontal mesh in the vertical direction. These variables reside within the 'full' vertical layers $k = 1, 2, \ldots, N_z$. Normally-oriented horizontal velocity components are positioned at the midpoints of the dual Delaunay edges $\mathbf{x}_e$ and sit on the midplane of each full vertical layer k. The vertical velocity components are staggered at the centres of the Voronoi polygons $\mathbf{x}_i$ and the half-level vertical layer interfaces $l = k \pm \frac{1}{2}$. The length of an edge e in the polygonal mesh is denoted l_e, the length of its orthogonal dual d_e and the areas of the cells and dual triangles A_i and A_v, respectively. These quantities are computed with respect to the geometry the flow is embedded in — Euclidean measures for planar problems, and spherical metrics for flows on the sphere. See Figure 1 for additional description of MPAS-Ocean's staggered mesh configuration.

https://doi.org/10.5194/egusphere-2024-472
Preprint. Discussion started: 27 February 2024

4 Spatial discretization

Integrating the continuous equations (5–8) over the layered, unstructured polygonal mesh defined previously leads to a discrete finite-volume type discretization, in terms of a layerwise continuity equation

$$\partial_t \iint \mathrm{d}A\,\mathrm{d}z' + \iint_{\Omega} \nabla\cdot\mathbf{u}\,\mathrm{d}A\,\mathrm{d}z' = \iint_{\Omega} s^h\,\mathrm{d}A\,\mathrm{d}z'\,, \tag{10}$$

$$\partial_t h_{i,k} + \mathrm{D}^h\,\overline{hu}_{e,k} + \left[\dot{z}_{i,k}\right|_{k+\frac{1}{2}}^{k-\frac{1}{2}} = S^h_{i,k}\,, \tag{11}$$

a discrete horizontal and vertical momentum

$$\partial_t u_{e,k} + \overline{qhu}^{\perp}_{e,k} + \left[\dot{z}_{i,k}\,\mathrm{G}^z\,u_{e,k}\right|_{k+\frac{1}{2}}^{k-\frac{1}{2}} = -\frac{1}{\rho_0}\,\mathrm{G}^h\left(p'_{i,k}+\pi_{i,k}\right) - \mathrm{G}^h\,K_{i,k} + S^u_{e,k}\,, \tag{12}$$

$$q = \frac{\xi+f}{h}, \qquad \xi = \nabla\times\mathbf{u}_h\,, \tag{13}$$

$$\partial_t w_{i,k} + \mathrm{D}^h\,\overline{wu}_{e,k} + \left[\dot{z}_{i,k}\,\mathrm{G}^z\,w_{i,k}\right|_{k+\frac{1}{2}}^{k-\frac{1}{2}} = -\frac{1}{\rho_0}\,\mathrm{G}^z\,\pi_{i,k} + S^w_{i,k}\,, \tag{14}$$

and a discrete tracer equation

$$\partial_t h_{i,k}\psi_{i,k} + \mathrm{D}^{\psi}\,\overline{\psi hu}_{e,k} + \left[\psi_{i,k}\dot{z}_{i,k}\right|_{k+\frac{1}{2}}^{k-\frac{1}{2}} = S^{\psi}_{i,k}\,. \tag{15}$$

The subscripts i and e indicate the discretized variables through cell centers and edges, respectively, the $\overline{x}$ symbol represents the averaging of a variable from its native location to an edge or vertex, and D and G are the divergence and gradient operator, respectively. The subscript k indicates the vertical layer, where $k=1$ is the top layer, and k increases downward. $\dot{z}_{i,k}$ represents the vertical transport through the layer interface, and an Arbitrary Lagrangian–Eulerian (ALE) algorithm is implemented for its computation. ALE offers a great deal of freedom to choose among vertical grid types. For z-level vertical coordinates, $\dot{z}_{i,k}$ is computed so that layer thicknesses remain constant for $k>1$. In z-star coordinates, $\dot{z}_{i,k}$ is computed so that sea surface height (SSH) perturbations are distributed throughout the column. For more details regarding the spacial discretization please refer to Ringler et al. (2013); Petersen et al. (2015).

4.1 Nonhydrostatic pressure field

At every instant in time, the nonhydrostatic pressure field is updated with

$$\pi^{n+1}_{i,k} = \pi^{n}_{i,k} + \delta\pi_{i,k} \tag{16}$$

where $\delta\pi$ is the nonhydrostatic pressure-correction. This method is termed the pressure-correction algorithm and it is second-order accurate in time, as demonstrated in section 6.2. The horizontal and vertical velocity fields are corrected with the nonhy-

https://doi.org/10.5194/egusphere-2024-472
Preprint. Discussion started: 27 February 2024

drostatic pressure-correction as

$$u_{e,k}^{n+1} = u_{e,k}^{*} - \Delta t \frac{1}{\rho_0} \mathrm{G}^h \, \delta\pi_{i,k} \tag{17}$$

$$w_{i,k}^{n+1} = w_{i,k}^{*} - \Delta t \frac{1}{\rho_0} \mathrm{G}^z \, \delta\pi_{i,k} \tag{18}$$

where u^* and w^* are the predicted velocity fields, which do not satisfy local continuity. The pressure-correction is computed solving a Poisson system and assuming that the velocity field is divergence-free at time step $n+1$, i.e.

$$\mathrm{D}\,\mathbf{u}^{n+1} = 0\,. \tag{19}$$

Adding (17) and (18) up and applying (19) yields to

$$-\frac{1}{\Delta t}\left(\mathrm{D}^h \, u_{i,k}^{*} + \mathrm{D}^z \, w_{i,k}^{*}\right) = -\frac{1}{\rho_0}\left(\mathrm{D}^h(\mathrm{G}^h \, \delta\pi_{i,k}) + \mathrm{D}^z(\mathrm{G}^z \, \delta\pi_{i,k})\right) \tag{20}$$

which can be re-written as

$$G^2 \delta\pi = \rho_0 \frac{1}{\Delta t} \mathrm{D}\,\mathbf{u}^{*}\,, \tag{21}$$

where $G^2 x = \mathrm{D}(\mathrm{G}\,x)$. We solve eq. (21) with the preconditioned conjugate gradient algorithm with the preconditioner described in Section 6.1. If the pressure field is hydrostatic, then $\delta\pi = 0$ and $u^{n+1} = u^*$. Boundary conditions on the nonhydrostatic pressure-correction are gradient-free at solid boundaries and $\delta\pi = 0$ at the free surface. At open boundaries, a no-gradient condition on the nonhydrostatic pressure is imposed. To handle bathymetry in our implementation, the matrix is expanded to include 'null rows' to represent land-masked layers, see Figure 2. This assures the matrix to be non-singular and allows to support dynamic-in-time vertical layering, that is cells can shift between masked and active throughout the simulation.

5 Numerical results

In this section the nonhydrostatic capability of MPAS-Ocean is assessed by different nonhydrostatic benchmark test cases. The test cases employed here are all 2D, and the RK4 time-stepping scheme has been used for their solution. The tests consists of: (1) a continuously stratified seiche in an enclosed domain, (2) the formation of internal solitary waves, (3) the generation of a plume in an overflow scenario, and (4) the formation of Kelvin–Helmholtz billows at the shear interface between two fluids of different densities.

5.1 Continuously-stratified internal seiche

In this test case we reproduce the behavior of an internal seiche following Vitousek and Fringer (2014). The domain has length $L = 10$m and depth $D = 16$m, and we discretize it using 64 grid points in the horizontal and 100 layers in the vertical. The initial horizontal velocity is zero, and the initial density stratification is given by

$$\rho(x,z,t=0) = \rho_0 + \frac{1}{2}\Delta\rho\Big[1 - \tanh\Big(\frac{2\tanh^{-1}(\alpha_s)}{\delta_p}(z + H/2 - \xi)\Big)\Big], \tag{22}$$

https://doi.org/10.5194/egusphere-2024-472
Preprint. Discussion started: 27 February 2024

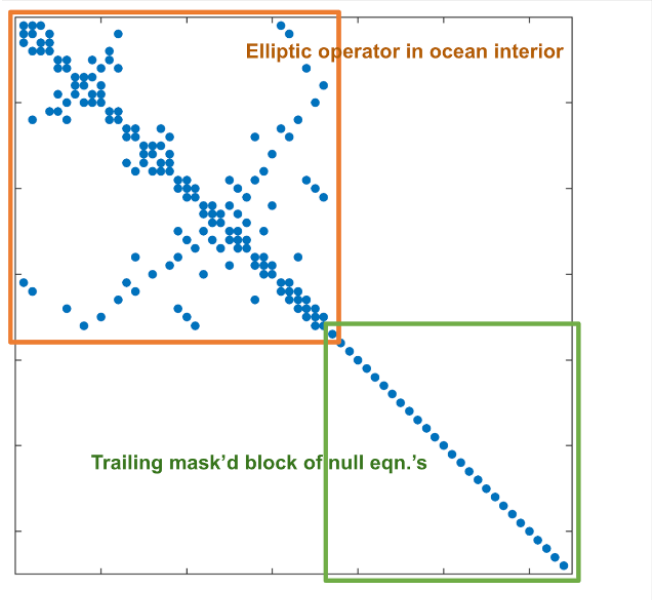

Figure 2. Sparsity pattern of nonhydrostatic elliptic operator, including land-masked block.

where $\alpha_s = 0.99$, $\delta_p = 1$m, $\rho_0 = 1000$kg m^3, and the density difference is given by $\Delta\rho/\rho_0 = 0.01$. For the interface height we use $\xi = a_i \cos(kx)$ where $a_i = 0.1$m. The hydrostatic and nonhydrostatic simulations are run without Coriolis force or vertical mixing for a total of 48s, which represents one period of oscillation. The RK4 time-step used is $\Delta t = 0.01$s, and the viscosity values in the horizontal and vertical momentum equations are $\nu_h = \nu_v = 0.01$ m^2 s^{-1}. To validate the new nonhydrostatic capability, we compare depth-profiles of the horizontal and vertical velocity in the nonhydrostatic and hydrostatic model. As described in Fringer et al. (2006), the velocity profiles are expected to resemble first-mode profiles computed with a linearized eigenfunction analysis (see Fringer and Street (2003)), specifically they are expected to decay exponentially with distance from the interface. This linear, nonhydrostatic effect, is correctly represented by the nonhydrostatic MPAS-Ocean simulation. Fig. 3 shows the horizontal and vertical velocity profiles normalized by their respective maxima at locations $x = L/2$ and $x = 0$, respectively. The plotted time is $t = T/4$, with T being the period of oscillation. As expected, the nonhydrostatic profiles decay with distance from the interface and so are in agreement with the first-mode velocity profiles. On the other hand, the hydrostatic solution approximates the seiche as a shallow water wave, and hence the velocity fields have a smooth variation near the stratified interface.

5.2 Internal solitary wave train

This test case approximates the evolution of solitary waves in the South China Sea following Vitousek and Fringer (2014); Zhang et al. (2011); Vitousek and Fringer (2011). The simulations are performed in a domain of length $L = 300$km and depth $H = 2000$m discretized with 1200 cells in the horizontal and 100 vertical layers. The initial horizontal velocity is zero, and the

https://doi.org/10.5194/egusphere-2024-472
Preprint. Discussion started: 27 February 2024

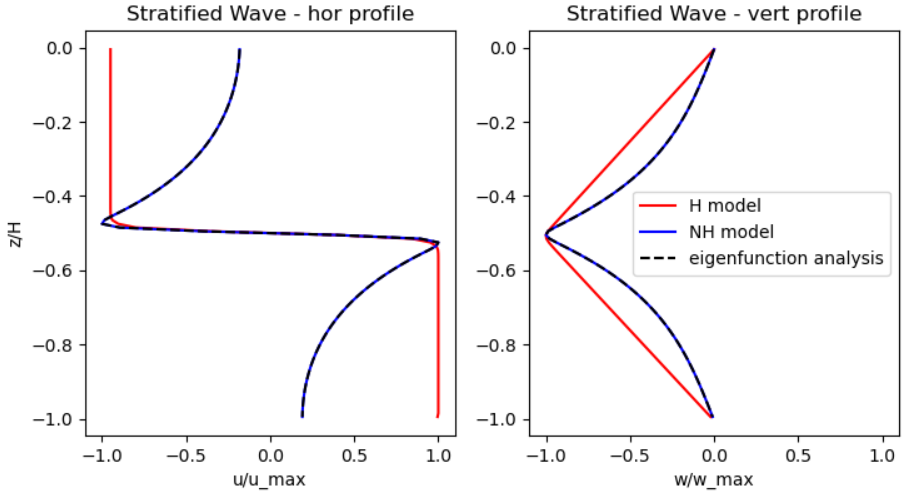

Figure 3. Horizontal and vertical velocity profiles of the internal seiche calculations at $t = T/4$ using the hydrostatic and nonhydrostatic solvers.

density stratification is given by

$$\rho(x,z,t=0) = \rho_0 - \frac{1}{2}\Delta\rho \tanh\left[\frac{2\tanh^{-1}(\alpha_s)}{\delta_p}(z - \xi(x,t=0) + h_1)\right], \tag{23}$$

where $\alpha = 0.99$, $\delta_p = 200$m, the upper-layer depth is $h_1 = 250$m, and the density difference is given by $\Delta\rho/\rho_0 = 0.001$ with $\rho_0 = 1000$kg m^3. The initial Gaussian depression that evolves into a train of solitary waves is given by

$$\xi(x,t=0) = -a_i \exp\left[-\left(\frac{x}{L_p}\right)^2\right], \tag{24}$$

with $a_i = 250$m and $L_p = 15$km. Figures 4 and 5 show the evolution of the solitary wave train for the hydrostatic and non-hydrostatic case, respectively. Both simulations are run without Coriolis force or vertical mixing for a total of 40 hours, with a time-step for the RK4 scheme of 1s. For the nonhydrostatic simulation we used $\nu_h = 0.1$ m^2 s^{-1} and $\nu_v = 0.01$ m^2 s^{-1}, whereas for the hydrostatic model a larger value of ν_h was needed to ensure stability, and we used $\nu_h = 10.0$ m^2 s^{-1}. In both cases, a wave is fully developed around 6 hours, and from that time the differences between the two models start to have an effect. The nonhydrostatic MPAS-Ocean simulation correctly shows that the single wave has broken into rank-ordered solitons at 24 hours, with the number of solitons increasing going further in time. As expected, the hydrostatic model fails to capture the correct physics, with the formation of a steep wave at 24 hours caused by a lack of dispersion in the hydrostatic model. This weak dispersion results in excessive numerical diffusion which leads to amplitude loss in the leading solitary-like wave as well as a thickening of the stratification in the lee of the wave train. The rapid oscillations that the hydrostatic case exhibits before the formation of the steep wave caused the need of a higher viscosity value as mentioned above.

By changing time-stepping scheme, the accuracy of the models is impacted. As shown in Figure 6, if we use a barotropic/baroclinic splitting scheme with a baroclinic time-step of 1m and a barotropic of 1s, the amplitude of the hydrostatic wave

https://doi.org/10.5194/egusphere-2024-472
Preprint. Discussion started: 27 February 2024

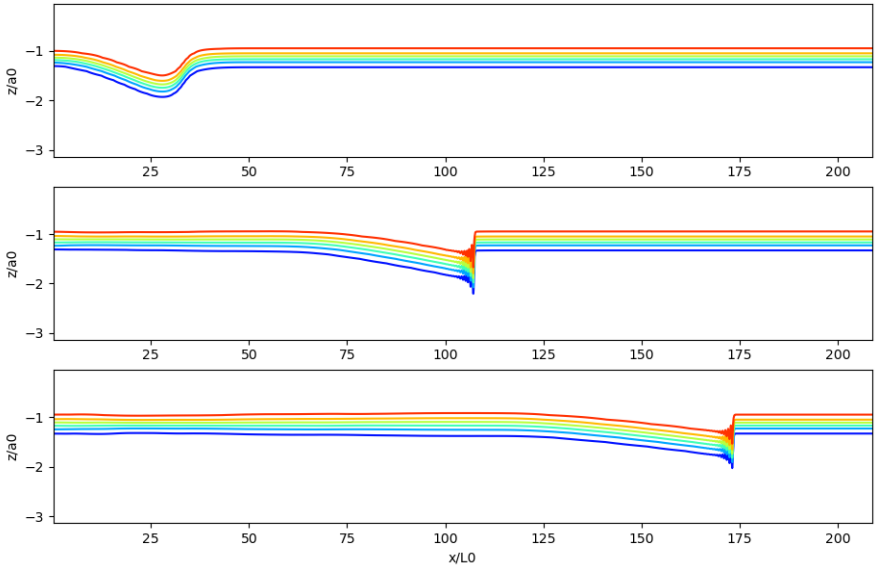

Figure 4. Evolution of the internal solitary wave train for the hydrostatic case. Density countours ploted at 6, 24 and 40 hours.

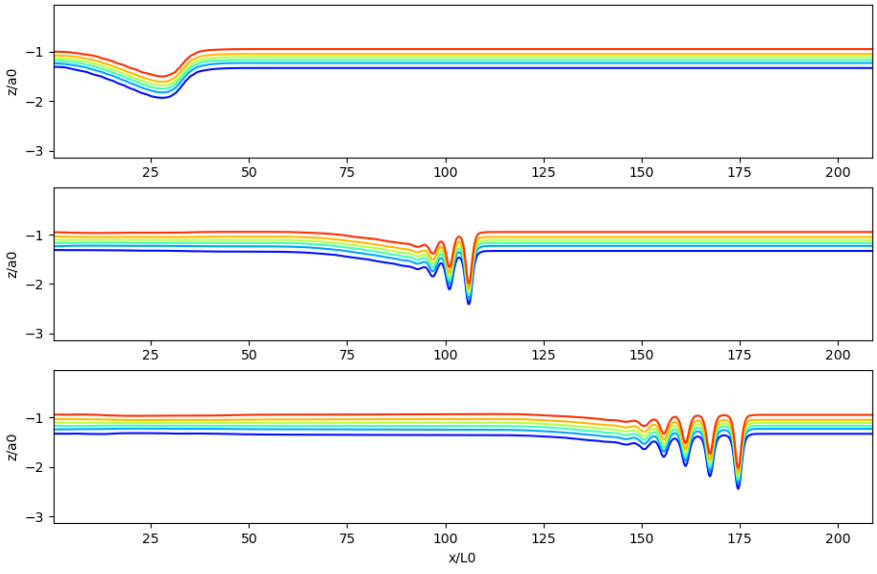

Figure 5. Evolution of the internal solitary wave train for the nonhydrostatic case. Density countours ploted at 6, 24 and 40 hours.

https://doi.org/10.5194/egusphere-2024-472
Preprint. Discussion started: 27 February 2024

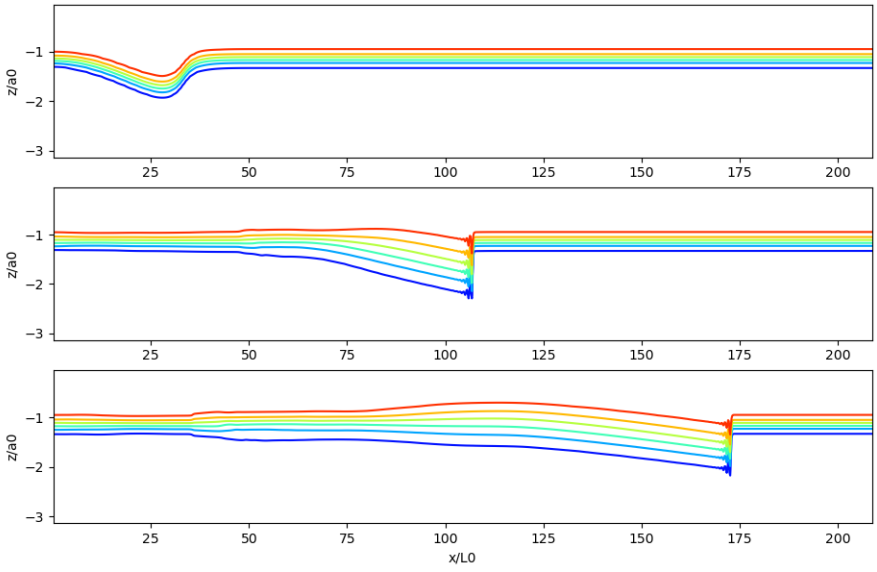

Figure 6. Evolution of the internal solitary wave train for the hydrostatic case using the split-implicit time-stepping scheme.

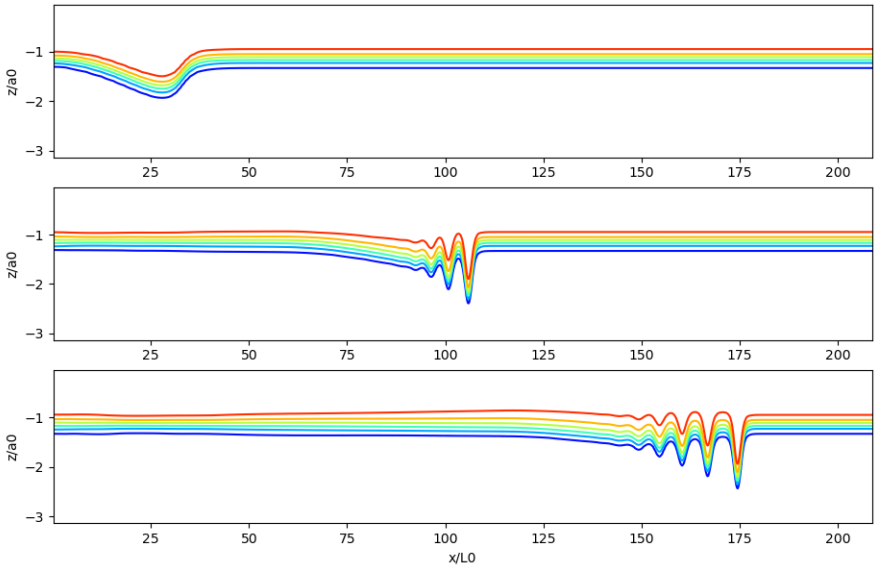

Figure 7. Evolution of the internal solitary wave train for the nonhydrostatic case using the split-implicit time-stepping scheme.

https://doi.org/10.5194/egusphere-2024-472
Preprint. Discussion started: 27 February 2024

drastically enlarges. In the nonhydrostatic case, the amplitude of the solitions is affected in a similar way (Figure 7). The reason is the underlining order of the time-stepping scheme, which is one for both split-explicit and split-implicit. Using a shorter baroclinic time-step of 15s, the solution obtained with the higher order RK4 is recovered with the splitting schemes as well.

It is important to notice that the leptic ratio $\Delta x/\Delta z$ plays a major role in the formation of the solitary waves for the nonhydrostatic case. As shown in Fig. 7 in Vitousek and Fringer (2011), for a large leptic ratio the nonhydrostatic and hydrostatic results are nearly identical. This is because increasing the grid lepticity causes the width of the leading solitary-like waves to grow in both the hydrostatic and nonhydrostatic solutions. With (horizontal) grid refinement, the width of the nonhydrostatic wave converges to the correct solution, whereas for the hydrostatic case the width continues to decrease because of a lack of dispersion. Therefore, high resolution grids are very important for the representation of the correct physics in nonhydrostatic simulations.

5.3 Nonhydrostaic overflow

This test case represents the flow of dense fluid down a slope. It is similar to the *Gravity Plume On a Continental Slope* test from MITgcm [plu], but we do not include any surface heat flux, instead our initial temperature field is a step function to induce convection. The domain has length $L = 6.4$km and depth $H = 200$m, and it is discretized with 320 cells in the horizontal and 60 layers in the vertical. The topography is given by

$$H(x) = -H_0 + \frac{1}{2}(H_0 - h_s)\left(1 + \tanh\left(\frac{x - x_s}{L_s}\right)\right), \tag{25}$$

where $s = 0.15$ is the maximum slope, $H_0 = 200$m is the maximum depth, $h_s = 40$m is the shelf depth, $x_s = 4700$m is the lateral position of the shelf-break, and $L_s = \dfrac{H_0 - h_s}{2s}$ is the length-scale of the slope. The initial temperature profile is

$$\Theta(x, z) = \begin{cases} 10 & x \leq 1\text{km}, \\ 20 & x > 1\text{km}, \end{cases} \tag{26}$$

so a denser fluid is initially present at the top of the slope. Both the hydrostatic and nonhydrostatic model are run without Coriolis force or vertical mixing for a total of 3 hours, with a time-step for the RK4 scheme of 0.5s. The viscosity values in the horizontal and vertical momentum equations are $\nu_h = \nu_v = 1$ m^2 s^{-1}. We compare the performance of the two models by looking at the temperature profiles over time. Figure 8 shows the dense fluid on the slope at times 20, 40, 60, 100, 140 and 180 minutes. At 20 min, the fluid is moving down the slope and we can see a plume forming in the nonhydrostatic case. At 40 min, the front is half way down the slope and the plume is fully developed. Its formation was possible because of the better physics representation in the nonhydrostatic model which allowed a Kelvin-Helmholtz instability to occur on the slope, leading to entrainment of ambient fluid into a plume. In the hydrostatic case, a steep wave has formed, similarly to the internal wave test case. After an hour, the fluid has reached the bottom of the slope, with the plume reaching its maximum amplitude. As the fluid moves away from the slope, we approach the shallow-water limit, meaning the horizontal scale becomes considerably larger than the vertical, and consequently the nonhydrostatic result starts to approach the hydrostatic one. As the fluid acceleration decreases so does the amplitude of the plume until, as we go further in time, the plume will resemble a steep wave.

https://doi.org/10.5194/egusphere-2024-472
Preprint. Discussion started: 27 February 2024

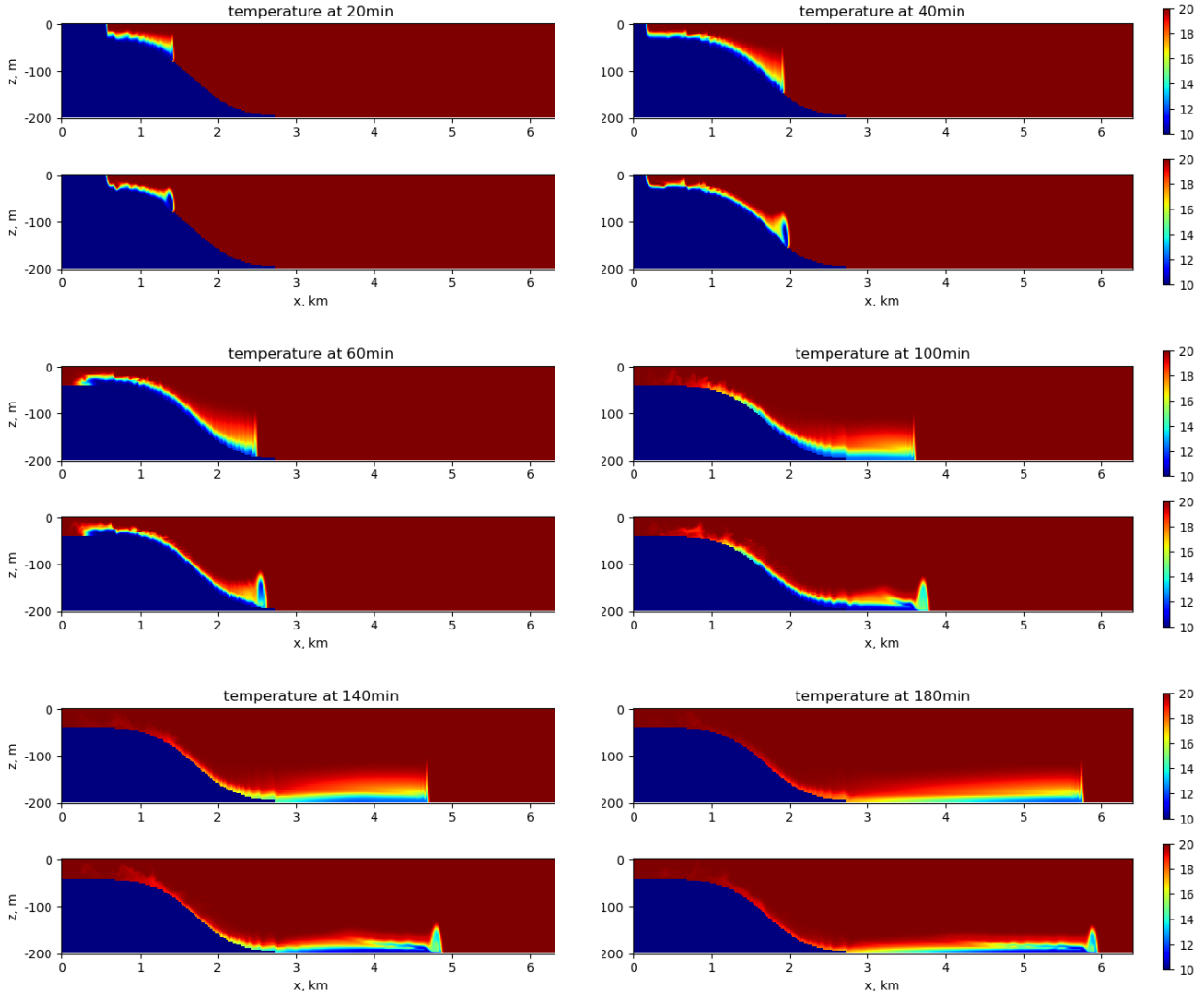

Figure 8. Nonhydrostatic overflow test case: temperature profiles for the hydrostatic (top) and nonhydrostatic (bottom) model at times 20, 40, 60, 100, 140 and 180 min.

https://doi.org/10.5194/egusphere-2024-472
Preprint. Discussion started: 27 February 2024

For all instants of time considered, the speed of the front is greater with the nonhydrostatic simulation, resulting in fluid locations that slightly vary for the two models. This is because a larger acceleration down the slope was possible in the nonhydrostatic case since vertical motions are better resolved.

5.4 Nonhydrostaic lock-exchange

This test may be thought of as two basins of water with different densities that are allowed to interact at time zero, producing an exchange flow. The domain is a rectangular tank with an horizontal length L of 0.5 m and a depth D of 0.1 m. We assume the bottom of the tank to be flat. The horizontal and vertical resolution are both 0.001 m. The initial density profile is

$$\rho(x,z) = \begin{cases} 1023.05 \text{ kg m}^{-3} & x \leq 0.25 \text{ m}, \\ 1026.95 \text{ kg m}^{-3} & x > 0.25 \text{ m} . \end{cases} \tag{27}$$

The viscosity values in the horizontal and vertical momentum equations are $\nu_h = \nu_v = 2\text{e}^{-6}$ m^2 s^{-1}. This is the only test case where Coriolis force and vertical mixing are active. Vertical background diffusion and viscosity are set to 1e^{-6} m^2 s^{-1}. For the tracer equation, horizontal diffusion is set to 2e^{-6} m^2 s^{-1}. We run the hydrostatic and nonhydrostatic model for 5s using the RK4 time-stepper with $\Delta t = 0.001$s. Figure 9 shows the density contours for the two runs, where we plotted ρ' = $\rho - 1000$ kg m^{-3}. As for the overflow case, a Kelvin-Helmholtz instability generates with the nonhydrostatic model which causes vigorous turbulent mixing to develop on the interface between high and low-density water. On the other hand, the hydrostatic simulation does not capture the generation of the Kelvin–Helmholtz billows. Because of the hydrostatic assumption, the density fronts cannot develop in the upper and lower layer.

6 Parallel Implementation

In this section, details about the MPAS-Ocean code performance are given. First, different preconditioners for the 3D Poisson equation are described and compared, all applied to a conjugate gradient algorithm. Second, the temporal accuracy of the nonhydrostatic formulation is investigated numerically, showing that the presented formulation is second-order accurate.

6.1 Nonhydrostatic solver

The liner system in (21) is solved with a preconditioned conjugate gradient (CG) algorithm using the external C++ library PETSc. PETSc, the Portable Extensible Toolkit for Scientific Computation, is a suite of data structures and routines for the parallel solution on high-performance computers of scientific applications modeled by partial differential equations [Balay et al. (2021a, b)]. We used the KSP package, which provides many popular Krylov subspace iterative methods, and the PC module, which includes a variety of preconditioners. We tested four types of preconditioners for CG: Jacobi, Additive Schwarz (AS), Block Jacobi with SOR on each block, and Block Jacobi with ILU on each bock. Jacobi uses a diagonal scaling and the

https://doi.org/10.5194/egusphere-2024-472
Preprint. Discussion started: 27 February 2024

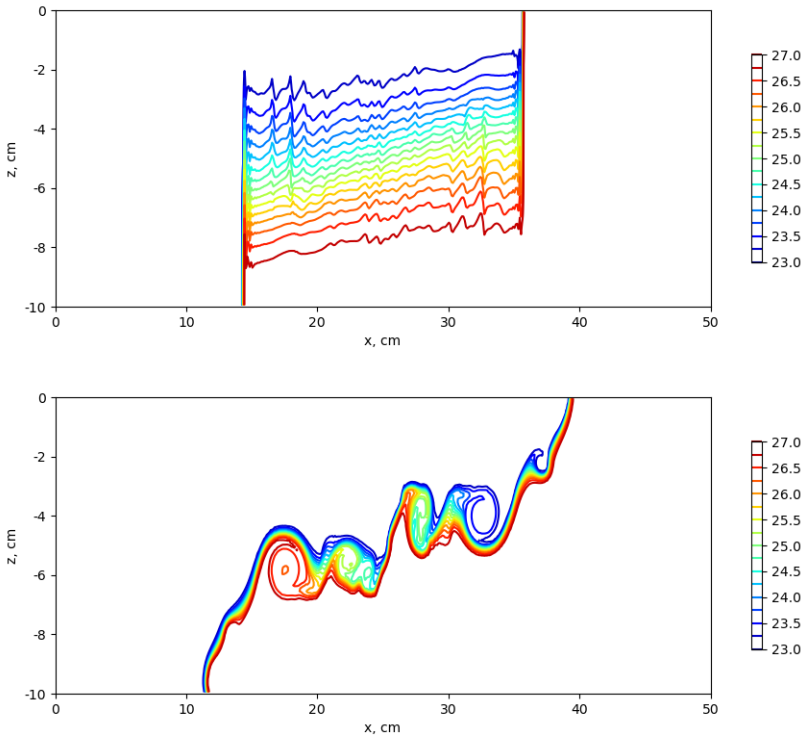

Figure 9. Density (ρ') contour plots at $t = 5$s for the lock-exchange test case.

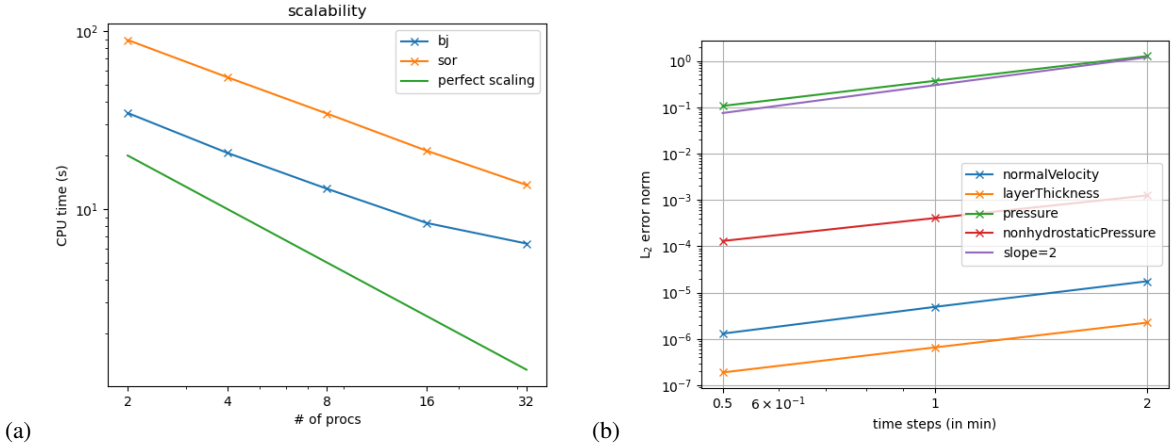

(a) (b)

Figure 10. (a) Processor scalability for the internal solitary wave test case; (b) temporal convergence for the internal solitary wave test case with the nonhydrostatic model.

https://doi.org/10.5194/egusphere-2024-472
Preprint. Discussion started: 27 February 2024

zero entries along the diagonal are replaced with the value 1.0. For AS we used the PETSc default, i.e. a restricted additive Schwarz method where the number of blocks is equal to the number of processors and the amount of overlap between blocks is set to 1.0. ILU is used for each block with a tolerance for zero pivot of 2.22 e^{-14}. For Block Jacobi, we tried two types of solvers for the blocks: SOR and ILU. The PETSC option PCSOR corresponds in parallel to block Jacobi with SOR on each block, whereas PCBJACOBI uses ILU as default for each block with a tolerance for zero pivot of 2.22 e^{-14}. The number of blocks corresponds once again to the number of processors. In terms of CPU time, Jacobi and AS showed the largest times for two different reasons. Jacobi, due to its simple strategy, takes a large number of iterations to achieve convergence (an average of 575 for the internal wave test case), whereas AS, despite taking the smallest number of iterations among the four preconditioning strategies, has the highest computational cost per iteration. PCSOR and PCBJACOBI perform best in terms of CPU time, with PCBJACOBI being the fastest of the two. Figure 10(a) shows their parallel efficiency obtained running the internal solitary wave test described in Section 5.2. The domain is discretized with 4800 cells in the horizontal, and the flow is integrated over a time interval of 1 hour using up to 128 processors. Both preconditioners show good scalability, with an average speedup of 1.6 every time the number of processes doubles.

6.2 Time accuracy

Here, we demonstrate second-order temporal accuracy of the nonhydrostatic formulation by performing numerical experiments. The internal wave test is simulated for 1 hour using the RK4 time-stepping scheme for the solution of the momentum and continuity equations. The nonhydrostatic pressure is updated at every time-step using equation (16), which is second-order accurate in time, and so despite using a fourth-order accurate time-stepper for the other variables, the accuracy of the overall time-stepping scheme is reduced to second-order. It is worth mentioning that if we were to use a first-order time-stepper for the solution of the momentum and continuity equations (as the split-explicit [Ringler et al. (2013)]), than the overall order of accuracy would drop to one, therefore it is important to use a second or higher order underling time-stepping scheme. To test that second-order is indeed achieved numerically, the flow is integrated over a time interval of 1 hour using three different time-step sizes, dt $= 2, 1$ and 0.5 s. The error is expressed as the L_2 norm of the difference between these solutions and a reference solution obtained with a time-step size of dt$= 0.01$ s. The error results for the horizontal velocity, fluid thickness, hydrostatic and nonhydrostatic pressure are shown in Figure 10(b). All errors converge with second-order accuracy. As in Fringer et al. (2006), we use the second-order Adams–Bashforth extrapolation scheme to compute the nonhydrostatic pressure at the final time step, i.e.

$$\pi_{\text{final}} = \frac{3}{2}\pi_{\text{last time-step}} - \frac{1}{2}\pi_{\text{second to last time-step}}\,. \tag{28}$$

This extrapolation is needed because the nonhydrostatic pressure is staggered in time with respect to the velocity, and failure to perform it results in a convergence rate of roughly 1.5 for the nonhydrostatic pressure term (not shown).

All benchmark tests presented in section 5 have been run successfully using the split-explicit [Ringler et al. (2013)] and semi-implicit [Kang et al. (2021)] algorithms as well. Both schemes are based on a barotropic/baroclinic splitting of the velocity, and their difference consists in the way the barotropic mode is solved. At this stage, the additional vertical momentum equation

https://doi.org/10.5194/egusphere-2024-472
Preprint. Discussion started: 27 February 2024

introduced by the nonhydrostatic model is solved using a forward Euler scheme with the baroclinic time-step, but in general nonhydrostatic effects may create fast vertical velocities that need smaller time-steps (or an implicit solver) to maintain stability. We indeed noticed that for the horizontal mixing in the vertical momentum equation a larger viscosity value (4 m^2 s^{-1} instead of 1 m^2 s^{-1}) was needed in the overflow test case in order to run the simulation stably with either splitting method. Future work will consist of investigating other strategies for the solution of the vertical momentum equation within a barotropic/baroclinic splitting scheme, with one possibility being the solution of the vertical momentum together with the barotropic mode. Our interest in using a barotropic/baroclinic splitting for the velocity is based on the larger time-steps than this strategy allows over explicit time discretizations, resulting in a significant reduction of the computational time.

7 Conclusions

For the correct resolution of highly convecting flows and submesoscale eddy processes along coastlines, the hydrostatic assumption usually adopted by ocean models does not do a good job in representing the physics of the problem, because of the shorter horizontal scales relative to the depth. In this work, we present a new formulation for MPAS-Ocean that solves the nonhydrostatic, incompressible Boussinesq equations, as opposed to its standard formulation that uses the hydrostatic assumption. We used a pressure-correcting projection method to extend the MPAS-Ocean hydrostatic model to a nonhydrostatic one, with the addition of a vertical momentum equation and a nonhydrostatic pressure term. A preconditioned conjugate gradient algorithm is employed for solving the 3D Poisson equation for the nonhydrostatic pressure using the external PETSc library. The nonhydrostatic formulation is shown numerically to be second-order accurate in time, as the nonhydrostatic pressure update is second-order. Four benchmark test cases are used to asses the new nonhydrostatic capability and they all show that MPAS-Ocean NH correctly represents nonhydrostatic effects in highly convective flows, as the multiscale internal wave energy cascade and the plume generation in an overflow scenario.

MPAS-Ocean NH is the first global nonhydrostatic model at variable resolution, and future work will consist in taking advantage of the variable resolution by implementing the capability of running the nonhydrostatic model only in defined high resolution regions of the domain. High resolution is necessary for the representation of nonhydrostatic effects, and the variable resolution mesh allows us to have appropriate high resolution in defined regions and much coarser regions elsewhere, making global simulations possible with a nonhydrostaic model. A nonhydrostatic model might play an important role for the resolution of convecting flows in areas as the Gulf of Mexico and the North Atlantic, therefore appropriate high resolution for the nonhydrostatic problem will be used on defined regions of the domain, where we expect strong vertical motions, whereas the hydrostatic model would be used in the majority of the domain. Furthermore, we will keep investigating strategies for the solution of the vertical momentum equation within a barotropic/baroclinic splitting scheme.

Code availability. MPAS-Ocean is an open-source code available on GitHub as part of the E3SM project: https://github.com/E3SM-Project/E3SM.

https://doi.org/10.5194/egusphere-2024-472
Preprint. Discussion started: 27 February 2024

Author contributions. Luke Van Roekel acquired the funds for the project leading to this publication, developed the initial model code and provided supervision. Darren Engwirda and Sara Calandrini optimized the model code. Sara Calandrini performed the simulations. Sara Calandrini prepared the manuscript with contributions from all co-authors.

Competing interests. The authors declare that they have no conflict of interest.

Acknowledgements. Research presented in this article was supported by the Laboratory Directed Research and Development program of Los Alamos National Laboratory under project number 20210289ER, and as part of the Energy Exascale Earth System Model (E3SM) project, funded by the U.S. Department of Energy, Office of Science, Office of Biological and Environmental Research Earth Systems Model Development Program area of Earth and Environmental System Modeling. The data was produced using a high-performance computing cluster provided by the DOE Office of Science, Office of Biological and Environmental Research Earth Systems Model Development Program area of Earth and Environmental System Modeling program and operated by the Laboratory Computing Resource Center at Argonne National Laboratory. This research also used resources provided by the Los Alamos National Laboratory Institutional Computing Program, which is supported by the U.S. Department of Energy National Nuclear Security Administration under Contract No. 89233218CNA000001.

https://doi.org/10.5194/egusphere-2024-472
Preprint. Discussion started: 27 February 2024

References

Gravity Plume On a Continental Slope, https://mitgcm.readthedocs.io/en/latest/examples/plume_on_slope/plume_on_slope.html#gravity-plume-on-a-continental-slope.

Auclair, F., Bordois, L., Dossmann, Y., Duhaut, T., Paci, A., Ulses, C., and Nguyen, C.: A non-hydrostatic non-Boussinesq algorithm for free-surface ocean modelling, Ocean Modelling, 132, 12–29, https://doi.org/https://doi.org/10.1016/j.ocemod.2018.07.011, 2018.

Balay, S., Abhyankar, S., Adams, M. F., Benson, S., Brown, J., Brune, P., Buschelman, K., Constantinescu, E., Dalcin, L., Dener, A., Eijkhout, V., Gropp, W. D., Hapla, V., Isaac, T., Jolivet, P., Karpeev, D., Kaushik, D., Knepley, M. G., Kong, F., Kruger, S., May, D. A., McInnes, L. C., Mills, R. T., Mitchell, L., Munson, T., Roman, J. E., Rupp, K., Sanan, P., Sarich, J., Smith, B. F., Zampini, S., Zhang, H., Zhang, H., and Zhang, J.: PETSc/TAO Users Manual, Tech. Rep. ANL-21/39 - Revision 3.16, Argonne National Laboratory, 2021a.

Balay, S., Abhyankar, S., Adams, M. F., Benson, S., Brown, J., Brune, P., Buschelman, K., Constantinescu, E. M., Dalcin, L., Dener, A., Eijkhout, V., Gropp, W. D., Hapla, V., Isaac, T., Jolivet, P., Karpeev, D., Kaushik, D., Knepley, M. G., Kong, F., Kruger, S., May, D. A., McInnes, L. C., Mills, R. T., Mitchell, L., Munson, T., Roman, J. E., Rupp, K., Sanan, P., Sarich, J., Smith, B. F., Zampini, S., Zhang, H., Zhang, H., and Zhang, J.: PETSc Web page, https://petsc.org/, https://petsc.org/, 2021b.

Calandrini, S., Engwirda, D., and Petersen, M.: Comparing numerical accuracy and stability for different horizontal discretizations in MPAS-Ocean, Ocean Modelling, 168, 101 908, 2021.

Casulli, V.: A semi-implicit finite difference method for non-hydrostatic, free-surface flows, International Journal for Numerical Methods in Fluids, 30, 425–440, https://doi.org/https://doi.org/10.1002/(SICI)1097-0363(19990630)30:4<425::AID-FLD847>3.0.CO;2-D, 1999.

Du, Q., Faber, V., and Gunzburger, M.: Centroidal Voronoi tessellations: Applications and algorithms, SIAM review, 41, 637–676, 1999.

Engwirda, D.: JIGSAW-GEO (1.0): locally orthogonal staggered unstructured grid generation for general circulation modelling on the sphere, Geoscientific Model Development, 10, 2117–2140, 2017.

Fringer, O., Gerritsen, M., and Street, R.: An unstructured-grid, finite-volume, nonhydrostatic, parallel coastal ocean simulator, Ocean Modelling, 14, 139–173, https://doi.org/https://doi.org/10.1016/j.ocemod.2006.03.006, 2006.

Fringer, O. B. and Street, R. L.: The dynamics of breaking progressive interfacial waves, Journal of Fluid Mechanics, 494, 319–353, 2003.

Golaz, J.-C., Caldwell, P. M., Van Roekel, L. P., Petersen, M. R., Tang, Q., Wolfe, J. D., Abeshu, G., Anantharaj, V., Asay-Davis, X. S., Bader, D. C., et al.: The DOE E3SM coupled model version 1: Overview and evaluation at standard resolution, Journal of Advances in Modeling Earth Systems, 11, 2089–2129, 2019.

Higdon, R. L.: A two-level time-stepping method for layered ocean circulation models: further development and testing, Journal of Computational Physics, 206, 463–504, 2005.

Hoch, K. E., Petersen, M. R., Brus, S. R., Engwirda, D., Roberts, A. F., Rosa, K. L., and Wolfram, P. J.: MPAS-Ocean Simulation Quality for Variable-Resolution North American Coastal Meshes, Journal of Advances in Modeling Earth Systems, 12, e2019MS001 848, https://doi.org/https://doi.org/10.1029/2019MS001848, e2019MS001848 10.1029/2019MS001848, 2020.

Kang, H.-G., Evans, K. J., Petersen, M. R., Jones, P. W., and Bishnu, S.: A Scalable Semi-Implicit Barotropic Mode Solver for the MPAS-Ocean, Journal of Advances in Modeling Earth Systems, 13, e2020MS002 238, 2021.

Klingbeil, K. and Burchard, H.: Implementation of a direct nonhydrostatic pressure gradient discretisation into a layered ocean model, Ocean Modelling, 65, 64–77, https://doi.org/https://doi.org/10.1016/j.ocemod.2013.02.002, 2013.

Marshall, J., Hill, C., Perelman, L., and Adcroft, A.: Hydrostatic, quasi-hydrostatic, and nonhydrostatic ocean modeling, Journal of Geophysical Research: Oceans, 102, 5733–5752, https://doi.org/https://doi.org/10.1029/96JC02776, 1997.

https://doi.org/10.5194/egusphere-2024-472
Preprint. Discussion started: 27 February 2024

Petersen, M. R., Jacobsen, D. W., Ringler, T. D., Hecht, M. W., and Maltrud, M. E.: Evaluation of the arbitrary Lagrangian–Eulerian vertical coordinate method in the MPAS-Ocean model, Ocean Modelling, 86, 93–113, 2015.

Petersen, M. R., Asay-Davis, X. S., Berres, A. S., Chen, Q., Feige, N., Hoffman, M. J., Jacobsen, D. W., Jones, P. W., Maltrud, M. E., Price, S. F., et al.: An evaluation of the ocean and sea ice climate of E3SM using MPAS and interannual CORE-II forcing, Journal of Advances in Modeling Earth Systems, 11, 1438–1458, 2019.

Ringler, T., Ju, L., and Gunzburger, M.: A multiresolution method for climate system modeling: Application of spherical centroidal Voronoi tessellations, Ocean Dynamics, 58, 475–498, 2008.

Ringler, T., Petersen, M., Higdon, R. L., Jacobsen, D., Jones, P. W., and Maltrud, M.: A multi-resolution approach to global ocean modeling, Ocean Modelling, 69, 211–232, https://doi.org/https://doi.org/10.1016/j.ocemod.2013.04.010, 2013.

Vitousek, S. and Fringer, O. B.: Physical vs. numerical dispersion in nonhydrostatic ocean modeling, Ocean Modelling, 40, 72–86, 2011.

Vitousek, S. and Fringer, O. B.: A nonhydrostatic, isopycnal-coordinate ocean model for internal waves, Ocean Modelling, 83, 118–144, https://doi.org/https://doi.org/10.1016/j.ocemod.2014.08.008, 2014.

Zhang, Z., Fringer, O., and Ramp, S.: Three-dimensional, nonhydrostatic numerical simulation of nonlinear internal wave generation and propagation in the South China Sea, Journal of Geophysical Research: Oceans, 116, 2011.